

Orbit topology analysed from π phase shift of magnetic quantum oscillations in three-dimensional Dirac semimetal

Sang-Eon Lee,¹ Myeong-jun Oh,² Sanghyun Ji,¹ Jinsu Kim,¹ Jin Hyun Jun,¹ Woun Kang,³ Younjung Jo,^{2,*} Myung-Hwa Jung^{1,†}

¹*Department of Physics, Sogang University, Seoul 04107, Korea*

²*Department of Physics, Kyungpook National University, Daegu 41566, Korea*

³*Department of Physics, Ewha Womans University, Seoul 03760, Korea*

Abstract

With the emergence of Dirac fermion physics in the field of condensed matter, magnetic quantum oscillations (MQOs) have been used to discern the topology of orbits in Dirac materials. However, many previous researchers have relied on the single-orbit Lifshitz–Kosevich formula, which overlooks the significant effect of degenerate orbits on MQOs based on the specific symmetry. This report demonstrates how spin-degenerate orbits affect the phases in MQOs of three-dimensional Dirac semimetal, NbSb₂. With varying the direction of the magnetic field, an abrupt π phase shift is observed due to the interference between the spin-degenerate orbits. We investigate the effect of cyclotron mass on the π phase shift and verify its close relation to the phase from the Zeeman coupling. We find that the π phase shift occurs when the cyclotron mass is 1/2 of the electron mass, indicating the effective spin gyromagnetic ratio is $g_s = 2$. Our approach is not only useful for analysing MQOs of Dirac semimetals with a small cyclotron mass, but also can be used for MQOs in materials with degenerate orbits, especially in correlated materials with a substantial cyclotron mass. Furthermore, this method provides a useful way to estimate the precise g_s value of the material.

* Corresponding authors. YJ (jophy@knu.ac.kr)

† Corresponding authors. MHJ (mhjung@sogang.ac.kr)

I. Introduction

Since the observation of the non-trivial π Berry phase obtained from magnetic quantum oscillations (MQOs) in the typical Dirac material of graphene, [1] the π phase in MQOs has become a signature of Dirac fermions. Subsequently, researchers have revealed Dirac fermions in topological insulators, [2–5] which possess Dirac cones in their surface electronic structures. [6–11] With the emergence of Dirac and Weyl semimetals, which have bulk electronic states that effectively manifest the Dirac and Weyl fermions, [12–17] the π phase in MQOs have been widely used to detect the topology of orbits. [18–23] As MQOs have been used for various topological materials, it seems problematic that many researchers still use the conventional single-orbit Lifshitz–Kosevich (LK) formula, whose form is $\cos(2\pi F/B - \pi + \lambda + \delta)$, for Shubnikov–de Haas (SdH) oscillation, where F is the frequency of the MQOs, B is the magnetic field, λ is the phase believed to manifest the Berry phase, and δ is the phase related to the Fermi-surface curvature. [19] [24] [25]

The orbit topology can be directly found using the conventional LK formula only for some special orbits, such as the orbits in graphene or the surface states of topological insulators. [26] For three-dimensional topological semimetals such as Dirac and Weyl semimetals, the effects of spin-orbit coupling and degenerate orbits are crucial, making it challenging to apply the conventional LK formula to discover the orbit topology. In this paper, we propose a methodology to analyse the MQOs of a Dirac semimetal. In general, a Dirac semimetal has two symmetries: time-reversal and spatial-inversion, which force the orbits to be spin-degenerate. If a magnetic field is applied, the energy levels of the spin-degenerate orbits will be split, and the split orbits will pick up the opposite phase. Consequently, the phase of a single orbit cannot be obtained directly, because only the phase of a superposed oscillation composed of the oscillations from two split orbits can be measured.

Recently, some studies have been conducted on the incorporation of spin-degenerate orbits. For instance, a π phase shift in MQOs that is dependent on the angle between the crystal axis and the magnetic field has been observed in ZrTe_5 , a three-dimensional Dirac semimetal. [27–30] The π shift was interpreted as the angle-dependent spin reduction factor, implying the interference between the oscillations from the spin-degenerate orbits. [30] Since ZrTe_5 is a quasi-two-dimensional material, [31] it has strong anisotropy, which may induce angle-dependent interference. Therefore, it is not clear whether the π phase shift can be observed in three-

dimensional (not quasi-two-dimensional) Dirac semimetals. Furthermore, the spin reduction factor used in the ZrTe₅ study only included the various phase contributions of the Berry phase and orbital magnetization in an effective gyromagnetic ratio. Thus, it cannot be known which is the origin of the π phase shift: the Berry phase, orbital magnetization, or Zeeman coupling.

For this purpose, we studied the MQOs of the massive Dirac semimetal NbSb₂, which is an electron-hole compensated semimetal with several band-touching points without spin-orbit coupling (the spin-orbit coupling splits the band touching points and opens the gaps). [32–34] To the best of our knowledge, this is the first time that the orbit topology has been determined for a Dirac semimetal considering degenerate orbits

II. Preliminary theory

The conventional means of determining orbit topology is to fit the measured MQOs with the conventional LK formula and obtain the phase information. Considering the superposed oscillation with spin-degenerate orbits, the form of the LK formula should be $\cos(2\pi F/B - \pi + \lambda + \delta) + \cos(2\pi F/B - \pi - \lambda + \delta) = 2 |\cos \lambda| \cos(2\pi F/B - \pi + \Theta + \delta)$, where $\Theta = \frac{\pi}{2}[1 - \text{sign}(\cos \lambda)]$, as shown in Ref. [26]. Incorporating the reduction factor and higher-order harmonics, the ratio of the oscillatory part of the conductivity $\Delta\sigma_{xx}$ to the non-oscillatory part σ_{xx}^{no} , $\Delta\sigma_{xx}/\sigma_{xx}^{no}$, for a three-dimensional Dirac semimetal is [19,25,26,35]

$$\frac{\Delta\sigma_{xx}}{\sigma_{xx}^{no}} \approx \sum_{p=1}^{\infty} A_{\sigma} \sqrt{B/p} R_T R_D |\cos p\lambda| \cos \left[p \left(\frac{2\pi F}{B} - \pi \right) + \Theta \pm \delta \right], \quad (1)$$

where A_{σ} is a dimensional constant, p is the harmonic order, $R_T = \frac{2\pi^2 p k_B T / \hbar \omega_c}{\sinh(2\pi^2 p k_B T / \hbar \omega_c)}$ is the temperature reduction factor, and $R_D = \exp(-\pi p / \tau \omega_c)$ is the Dingle reduction factor. The first problem with the conventional method of determining orbit topology is that only the phase Θ can be obtained, not λ . The second problem is that even if λ is obtained from Θ , λ is not the Berry phase, but rather is composed of three phases, i.e., $\lambda = \phi_B + \phi_R + \phi_Z$, where ϕ_B , ϕ_R , and ϕ_Z are related to the Berry phase, the orbital magnetization, and the Zeeman coupling,

respectively. If λ is close to 0 (π), the orbit has a trivial (non-trivial) topology. In this paper, we discuss how λ can be obtained from Θ and how the orbit topology can be obtained from λ .

III. Results and discussion

We measured the magnetoresistance (MR) of NbSb₂ with varying the angle θ between the current direction (b-axis) and the direction of the magnetic field [see the inset of Fig. 1(a)]. The elongated direction of the sample is along the b-axis. [32,33] Fig. 1(a) shows the MR curves of NbSb₂ from $\theta = -90^\circ$ to $\theta = 90^\circ$. The MR gradually increases with increasing $|\theta|$. When the magnetic field is applied perpendicular to the current direction ($\theta = \pm 90^\circ$), an extremely large MR is evident ($\sim 1.8 \times 10^6\%$ at 14 T and 1.5 K), which exceeds previously reported MR values. [32,33] In semimetals such as NbSb₂, the large MR is attributed to the almost perfectly compensated carrier density and high crystal quality. [33,36,37–39] To estimate the carrier density, we measured the Hall resistance of NbSb₂ and fit the data with a two-carrier model. Consequently, we obtain an almost compensated carrier density (Supplementary Fig. S3). The compensated carrier density is well matched with the previous density functional theory calculation results. [34] Furthermore, the high crystal quality is manifested in the high residual resistivity ratio (RRR) of ~ 520 (Supplementary Fig. S3), which is higher than the values reported previously. [32,33]

SdH oscillations are clearly observable in the MR data. We analysed these oscillations using a fast Fourier transform (FFT). Fig. 1(b) shows the typical FFT amplitude of the oscillations at $\theta = 60^\circ$. We define the peaks in Fig. 1(b) as α and β oscillations and their second harmonics as 2α and 2β . The frequencies of the α and β oscillations are similar to those reported previously [32,33] Fig. 1(c) presents the angle-dependent FFT frequencies of the SdH oscillations, including the major α (black closed circles) and β (red closed circles) oscillations and their second harmonics (black and red open circles) as well as the minor ζ (magenta stars) and η (cyan rhombuses) oscillations. The overall behaviour of the angle-dependent frequencies is symmetric to $\theta = 0^\circ$, where the applied magnetic field is along the two-fold symmetric axis of the crystal (b-axis). The α and β oscillations span all angles and monotonically vary with the angle, whereas the ζ and η oscillations are observable for only a small range of angles.

In order to analyse the MQOs in detail, we convert the conductivity form in equation (1) into the form of resistivity using the recent transport theory for MQOs [40] (Supplementary Section 3). We obtain the form of inverse resistivity, $\Delta\rho_{xx}^{-1}/\rho_{xx}^{no-1} \approx \sum_i f_i \varepsilon_i$ by introducing a correction factor f_i which is added to the oscillatory part of the conductivity from the i th carrier ε_i . Consequently, we obtain

$$\frac{\Delta\rho_{xx}^{-1}}{\rho_{xx}^{no-1}} \approx \sum_i \sum_{p=1}^{\infty} A_{p,i} \sqrt{B/p} R_{T,i} R_{D,i} |\cos p\lambda_i| |f_i| \cos \left[p \left(\frac{2\pi F_i}{B} - \pi \right) + \Theta_i \pm \delta_i + \varphi_i \right], \quad (2)$$

where $A_{p,i}$ is a dimensional constant. We introduce the phase $\varphi_i = \frac{\pi}{2} [1 - \text{sign}(f_i)]$. If f_i is positive (negative), the phases of inverse resistivity and conductivity are the same (differ by π). Furthermore, the shape of the oscillations can be modified if f_i changes the sign with varying the magnetic field. Supplementary Section 4 shows how f_i affects the phase and the amplitude of MQOs.

From the polynomial fits of the measured MR curves, we obtain the non-oscillatory and oscillatory parts of the resistance and convert them into the form of inverse resistivity, $\Delta\rho_{xx}^{-1}/\rho_{xx}^{no-1}$. We select the frequency range encompassing the α and β oscillations [red shaded area in Fig. 1(b)] and filter out all other frequencies. The upper panel of Fig. 1(d) shows the filtered data and the fitted curve obtained from equation (2) (here, we set $|f_i| = 1$). The agreement between them justifies applying the LK theory to the filtered data. The α and β oscillations are well reconstructed separately from the fitted curve, as shown in the lower panel of Fig. 1(d).

Now, we discuss the amplitude and the phase obtained from the above analyses. Although we attempted to analyse both α and β oscillations, it was impossible to solely resolve the β oscillations because the frequency of the β oscillations is too close to those of the other oscillations to apply the FFT band-pass filter [Fig. 1(c)]. Thus, we focus on the α oscillations and analyse the amplitude and the phase. In Fig. 2(a), we plot the FFT amplitudes of the α oscillations and the 2α oscillations, $A(\alpha)$ and $A(2\alpha)$, respectively. For most angles, $A(\alpha)$ is much larger than $A(2\alpha)$, except at $\theta = \pm 40^\circ$ where $A(\alpha)$ becomes very small, even smaller than $A(2\alpha)$. The phases of the α oscillations are obtained by drawing the Landau-level fan diagram (see Supplementary Fig. S5, S6). As is conventionally done [1,21,30], we divide the obtained phase of the α oscillations by 2π , which is written as $\gamma_\alpha = (-\pi + \Theta_\alpha \pm \delta_\alpha + \varphi_\alpha)/2\pi$. Fig. 2(b) represents $A(2\alpha)/A(\alpha)$ and γ_α as a function of θ . Interestingly, γ_α abruptly

changes by 0.5 (corresponding to π phase shift) near $\theta = \pm 40^\circ$, where $A(2\alpha)/A(\alpha)$ increases. Here, we do not present an analysis of the α oscillations at $\theta = -10^\circ$ – 10° , where the η oscillations are close to the α oscillations. And the detailed analysis for another omitted data at $\theta = \pm 90^\circ$ is in Supplementary Section 4. In equation (2), the related amplitude factors are $|\cos p\lambda_\alpha|$ and $|f_\alpha|$. However, the behaviour of the amplitudes at $\theta = \pm 40^\circ$ is different between the fundamental harmonics ($p = 1$) and the second harmonics ($p = 2$); hence, the p -dependent amplitude factor $|\cos p\lambda_\alpha|$ should be related. Since the factor is the cosine function, the observed large $A(2\alpha)/A(\alpha)$ is attributable to the fact that λ_α is close to $(n + 1/2)\pi$, where n is an integer. The phase factor related to λ_α is $\Theta_\alpha = \frac{\pi}{2}[1 - \text{sign}(\cos \lambda_\alpha)]$, and one can recognize that when λ_α is close to $(n + 1/2)\pi$, Θ_α is shifted by π .

In addition to the SdH oscillations, we measured the dHvA oscillations of NbSb₂ to check how well the oscillations match each other and how much the above analysis is reliable. Fig. 3(a) shows the FFT contour map of the dHvA oscillations, and the oscillations are defined as done in Fig. 1(c). The small difference of the frequency between the SdH and dHvA oscillations are most likely due to small misalignment in the measurement. Regarding the conductivity oscillations, the oscillatory part of the dHvA oscillations ΔM is given by [19,25,26]

$$\Delta M \approx \sum_i \sum_{p=1}^{\infty} -A_{M,i} \sqrt{B/p} R_{T,i} R_{D,i} |\cos p\lambda_i| \sin \left[p \left(\frac{2\pi F_i}{B} - \pi \right) + \Theta_i \pm \delta_i \right], \quad (3)$$

where $A_{M,i}$ is a dimensional constant. The phase Θ_i of the dHvA oscillations is obtained, and the phase parameter is defined as $\gamma'_i = (-\pi + \Theta_i \pm \delta_i)/2\pi$ (see Supplementary Fig. S7, S8). We compare the phase γ'_β to the FFT amplitude ratio $A(2\beta)/A(\beta)$ in Fig. 3(b). Similar to the SdH oscillations in Fig. 2(b), the π phase shift occurs near $\theta = 40^\circ$, where $A(2\beta)/A(\beta)$ increases, indicating that λ_β produces the π phase shift. As aforementioned, this phase shift is not necessary to be the Berry phase but is composed of three phases; $\lambda = \phi_B + \phi_R + \phi_Z$ where ϕ_B , ϕ_R , and ϕ_Z are related to the Berry phase, the orbital magnetization, and the Zeeman coupling, respectively. If λ is close to 0 (π), the orbit has a trivial (non-trivial) topology.

Next, we discuss the origin of the π phase shift. For this purpose, we assume that the predominant properties of the orbit can be determined by considering only two bands (called as two-band approximation). Previous theoretical works based on this assumption have shown that $\phi_B + \phi_R$ is approximately fixed to either 0 or π . [24,26]

Since the value of $\phi_B + \phi_R$ indicates the number of band touching points that the orbit encloses, when the number is even (odd), the value is zero (π). Therefore, we obtain $\lambda \approx \phi_Z$ or $\pi + \phi_Z$, so that the only possible origin of the amplitude-dependent π phase shift in our case is ϕ_Z resulting that the π phase shift occurs when $\phi_Z = (n + 1/2)\pi$.

The π phase shift is related to the cyclotron mass, which enables determining the orbit topology. We measured the temperature-dependent dHvA oscillations at some specific angles of $\theta = 0^\circ$, 40° , and 90° to estimate the cyclotron mass. The temperature-dependent FFT amplitudes of the oscillations at $\theta = 40^\circ$ is plotted in Fig. 4(a) (Supplementary Fig. S9 presents the data corresponding to the other angles), where the ζ , α , β , and 2β oscillations are shown. It is clearly seen that the amplitude decreases with increasing temperature. Notably, the amplitude of the 2β oscillations is larger than that of the β oscillations, indicating the π phase shift at this angle. Fig. 4(b) depicts the temperature-dependent amplitudes of the β oscillations for $\theta = 0^\circ$, 40° , and 90° , which are well fitted by using the temperature reduction factor R_T . The cyclotron mass is estimated to be $m_c = 0.52m_e$, $0.48m_e$, and $0.37m_e$, respectively. Since ΔM is smoothly varying with θ , it seems that the π phase shift occurring near $\theta = 40^\circ$ is related to $m_c \approx 0.5m_e$.

To understand the significance of the π phase shift when $m_c \approx 0.5m_e$, we should look at ϕ_Z . Roughly speaking, ϕ_Z indicates the relative size of the Zeeman energy splitting of an orbit compared to the Landau level splitting.

Since the Landau level splitting decreases with increasing the cyclotron mass, ϕ_Z is proportional to the cyclotron

mass; $\phi_Z = \pi \frac{g_s m_c}{2m_e}$, where g_s is the effective gyromagnetic ratio of the spin. [24,41] In general, the g_s is not

exactly 2 because of the effect of the spin-orbit coupling. However, for the β oscillations, since the frequency of the MQOs is relatively high between 400 and 700 T, one can suppose that the energy difference between the Fermi level and the band edge is large. Thus, the kinetic energy of the electrons at the Fermi level is high and will dominate the spin-orbit coupling energy, which corresponds to $g_s \approx 2$, leading to $\phi_Z = \pi \frac{m_c}{m_e}$. With this expression,

λ can be written as a function of m_c ; $\lambda = \pi \frac{m_c}{m_e}$ for a trivial orbit and $\lambda = \pi \left(1 + \frac{m_c}{m_e} \right)$ for a non-trivial orbit.

Finally, integrating the above statements, we discuss the orbit topology of the β oscillations. At $\theta = 90^\circ$, from $m_c = 0.37m_e$ we obtain $0 < \phi_z < \frac{1}{2}\pi$. The fact that the only possible values of $\phi_B + \phi_R$ are 0 or π results in $0 < \lambda < \frac{1}{2}\pi$ for $\phi_B + \phi_R = 0$ and $\pi < \lambda < \frac{3}{2}\pi$ for $\phi_B + \phi_R = \pi$. In this case, from $\Theta = \frac{\pi}{2}[1 - \text{sign}(\cos \lambda)]$, $\Theta = 0$ for $\phi_B + \phi_R = 0$ and $\Theta = \pi$ for $\phi_B + \phi_R = \pi$, which means that Θ and $\phi_B + \phi_R$ are the same, and we can find the orbit topology based on the measured value of Θ . From $\gamma_\beta = (-\pi + \Theta_\beta \pm \delta_\beta)/2\pi \approx 0.35$ for the β oscillations at $\theta = 90^\circ$ [Fig. 3(b)], $\Theta_\beta \approx 1.7\pi \mp \delta_\beta \pmod{2\pi} = -0.3\pi \mp \delta_\beta$. Plugging in $\delta_\beta \approx 0.25\pi$ [13,31], from $\Theta \approx 0$, we obtain $\phi_B + \phi_R \approx 0$, which means that the orbit producing β oscillations encloses an even number of band-touching points (assuming that the oscillations come from the maximum cross-section areas to determine δ_β). To the best of our knowledge, this is the first time that the orbit topology has been determined for a Dirac semimetal considering degenerate orbits. All the above discussion can be reproduced from the second harmonic of the β oscillations, 2β with twice the cyclotron mass, and the results are consistent (see Supplementary Section 7). It is noteworthy that the π phase shift will not occur at $m_c \approx 0.5m_e$ if one of the assumptions (the two-band approximation or $g_s \approx 2$) is not valid. We found this situation to be the case for the ζ oscillations, and Supplementary Section 7 provides the related discussion.

The results demonstrate that our method is suitable for analysing the MQOs in Dirac semimetals. Unlike the phase of the MQOs in graphene or the surface states of topological insulators, which is the Berry phase, the phase of the MQOs in Dirac semimetals must be analysed more carefully because of its spin-degenerate orbits and complex phase contributions. Equations (1)-(3) constitute the most suitable means for analysing the MQOs in Dirac semimetals. We measured the SdH and dHvA oscillations of the massive Dirac semimetal NbSb₂ and analysed the MQOs using the aforementioned equations. Both types of oscillations clearly showed π phase shifts, which are the manifestations of spin-degenerate orbits. We verified that the origin of the π phase shift observed in the dHvA oscillations is the Zeeman coupling, not the Berry phase. Most importantly, we determined the orbit topology using the method that considered the spin-degenerate states, which completely differs from the conventional method used for graphene or the surface state of a topological insulator. Not only will our approach

be useful to analyse the MQOs of Dirac semimetals, but it will also provide perspectives for analysing the MQOs of materials with strong spin-orbit coupling and degenerate orbits.

IV. Methods

Sample characterization. Single crystals of NbSb₂ were grown using chemical vapor transport, as reported previously. [42] First, polycrystalline NbSb₂ was synthesized by heating a stoichiometric mixture of high-purity Nb powder (99.99%) and ground Sb shot (99.9999%) in a vacuum-sealed quartz tube. The temperature was rapidly increased to 600 °C. Next, the temperature was slowly increased (2.5 °C/h) from 600 °C to 700 °C to prevent rapid melting of Sb and maintained at 700 °C for 36 h. Then, 1 g of the synthesized polycrystalline sample with iodine (10 mg/cc) was sealed under a vacuum in another quartz tube. Finally, the quartz tube was placed in a two-zone furnace and heated for 7 days. During heating, the end of the quartz tube containing the sample was maintained at 1000 °C, while the other end was kept at 900 °C. The quality and orientation of each sample were characterized using Powder and single-crystal X-ray diffractions. All the samples exhibited monoclinic (space group *C12/m1*) symmetry, confirming that the lattice parameters of our samples are similar to those reported previously (Supplementary Fig. S1).³⁸ The crystal structure of NbSb₂ is shown in Supplementary Fig. S2.

Quantum oscillations. Magnetotransport measurements using a standard four-probe method were carried out in high fields up to 14 T. Magnetization was measured in a magnetic field of 7 T using a commercial magnetic property measurement system (MPMS, Quantum Design). To quantify the complex oscillatory spectra of quantum oscillations, we used a fast Fourier transform (FFT) after removing a monotonic polynomial background from the raw data. When we found a clear peak in the FFT amplitude plot, we select two nearest minima (left and right) for the peak and set the minima as the boundary of an FFT band-pass filter. Individual oscillations are extracted separately using the FFT band-pass filter, as shown in Figs. 1(b)-(d) and Supplementary Figs. S5 and S7.

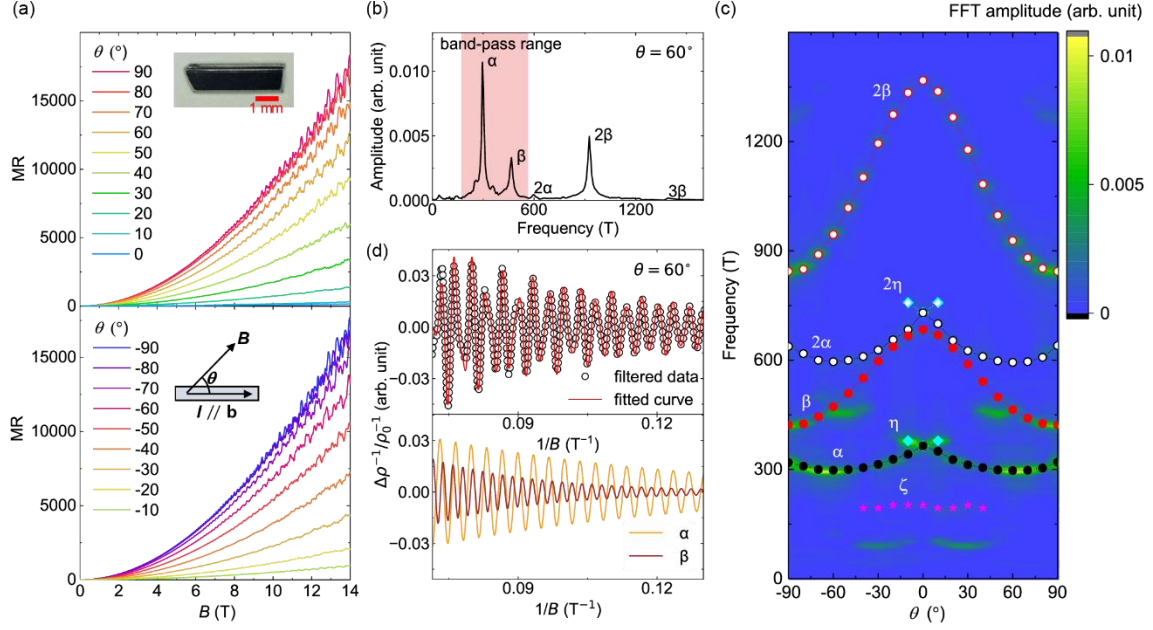


FIG. 1. MR and SdH oscillations of NbSb₂. (a) MR of NbSb₂ at $\theta = -90^\circ$ – 90° . The current direction is along the crystal b -axis, and θ is defined as the angle between the current and magnetic field directions. The insets in a show the picture of the crystal (upper panel) and the experimental configuration (lower panel). The extremely large MR of $1.8 \times 10^6\%$ (at 14 T and 1.5 K) is observable when the current is perpendicular to the magnetic field ($\theta = \pm 90^\circ$). (b) FFT data of NbSb₂ at $\theta = 60^\circ$. The α and β oscillations, second harmonic 2α and 2β oscillations, and third harmonic 3β oscillations are defined. The red shaded area shows the FFT band-pass filter range used to filter the α and β oscillations. (c) Angle-dependent FFT frequencies. The overall behaviour of the angle-dependent frequencies is symmetric to $\theta = 0^\circ$ where the applied magnetic field is along the two-fold symmetric axis of the crystal (b -axis). Additionally, the ζ and η oscillations are defined. (d) Filtered data (data in the band-pass range in b) and fitted curve obtained using equation (2). The agreement between filtered data and the fitted curve shows that it is suitable to apply the LK theory (upper panel). Reconstructed α and β oscillations obtained from the fitted curve in the upper panel (lower panel).

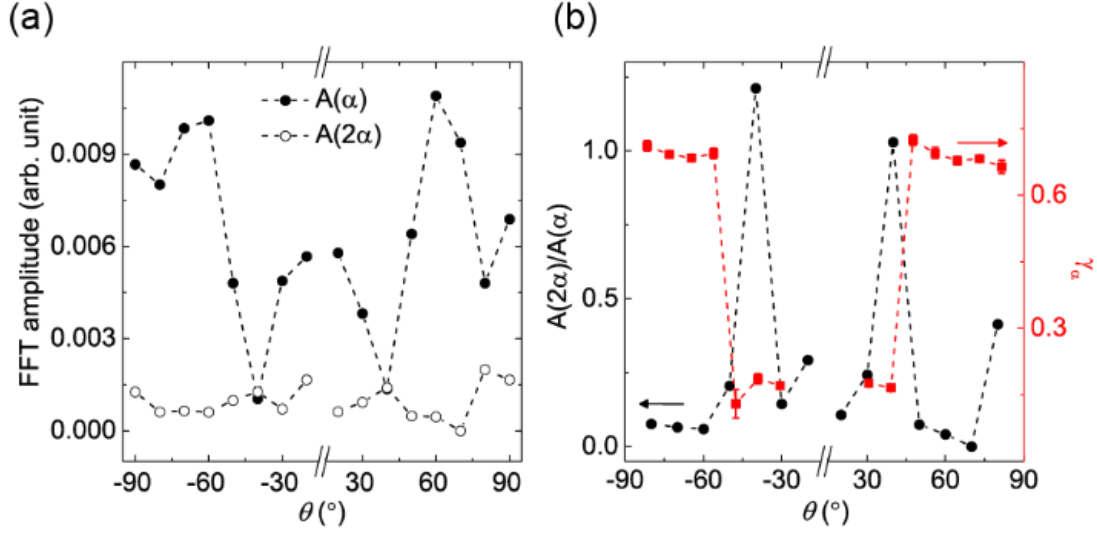


FIG. 2. Angle-dependent FFT amplitudes and phases of α oscillations in the SdH oscillations of NbSb₂. (a) Angle-dependent amplitudes of α oscillations $A(\alpha)$ and second harmonic 2α oscillations $A(2\alpha)$. $A(\alpha)$ is small at $\theta = \pm 40^\circ$ and even smaller than $A(2\alpha)$. (b) Angle-dependent amplitude ratio $A(2\alpha)/A(\alpha)$ and phase of α oscillations γ_α . γ_α abruptly changes by 0.5 (corresponding to π phase shift) near $\theta = \pm 40^\circ$, where the value of $A(2\alpha)/A(\alpha)$ increases. The coincidence between the large $A(2\alpha)/A(\alpha)$ and the π phase shift indicates that the π phase shift originates from the angle-dependent interference between the spin-degenerate orbits. The error bars manifest the standard error from the Landau fan diagram fitting.

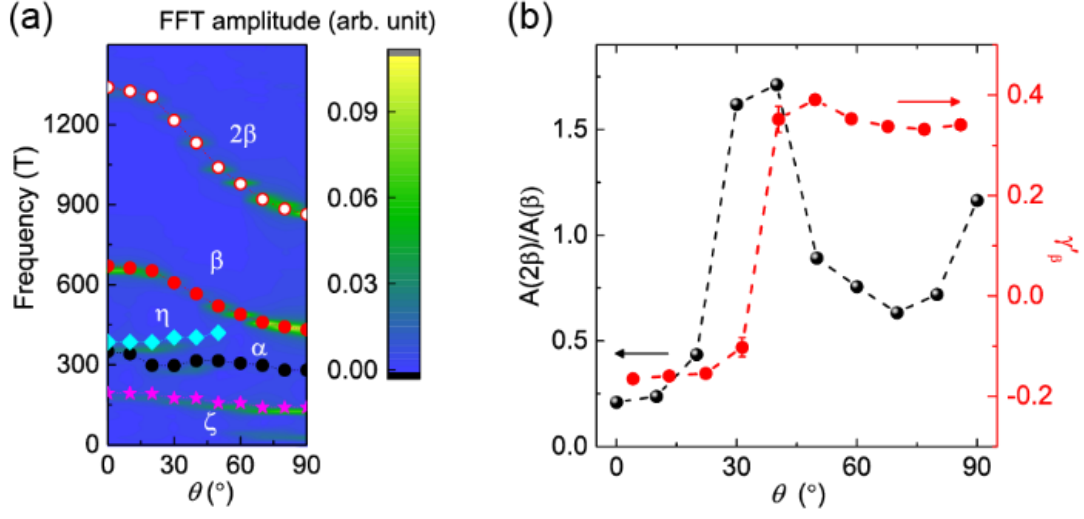


FIG. 3. Angle-dependent frequencies, amplitudes, and phases of dHvA oscillations in NbSb₂. (a) Angle-dependent frequencies of dHvA oscillations. α , β , ζ , and η oscillations are defined. (b) Angle-dependent amplitude ratios $A(2\beta)/A(\beta)$ and phase of β oscillations γ_β . γ_β abruptly changes by 0.5 (corresponding to π phase shift) near $\theta = 40^\circ$, where the value of $A(2\beta)/A(\beta)$ increases.

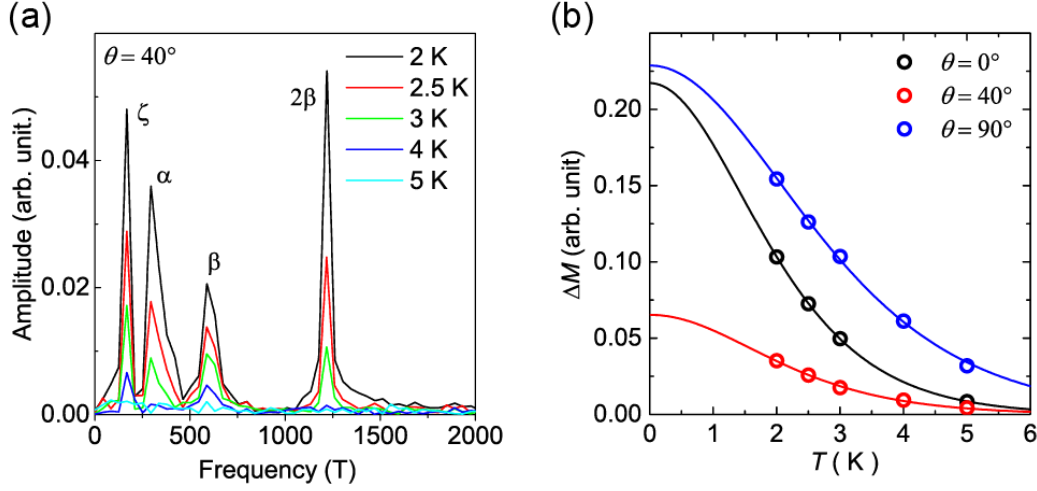


FIG. 4. Temperature-dependent dHvA amplitudes of NbSb₂. (a) FFT amplitude of dHvA oscillations at $\theta = 40^\circ$.

The amplitudes decrease with increasing temperature, which could be interpreted by the temperature reduction

factor $R_T = \frac{2\pi^2 p k_B T / \hbar \omega_c}{\sinh(2\pi^2 p k_B T / \hbar \omega_c)}$. [25] (b) Temperature-dependent FFT amplitudes of β oscillations at $\theta = 0^\circ$,

40° , and 90° (open symbols). The amplitudes are fitted with R_T (solid lines) for the cyclotron mass evaluation.

The cyclotron mass is evaluated to be $m_c = 0.52m_e$, $0.48m_e$, and $0.37m_e$ at $\theta = 0^\circ$, 40° , and 90° , respectively.

Acknowledgements

This work was supported by the National Research Foundation of Korea (NRF) grant (Nos. 2020R1A2C3008044, 2019R1A2C1089017 and 2018R1D1A1B07050087).

References

- [1] Y. Zhang, Y. W. Tan, H. L. Stormer, and P. Kim, *Experimental observation of the quantum Hall effect and Berry's phase in graphene*, Nature **438**, 201 (2005).

- [2] A. A. Taskin, S. Sasaki, K. Segawa, and Y. Ando, *Manifestation of Topological Protection in Transport Properties of Epitaxial Bi_2Se_3 Thin Films*, Phys. Rev. Lett. **109**, 066803 (2012).
- [3] A. A. Taskin and Y. Ando, *Berry phase of nonideal Dirac fermions in topological insulators*, Phys. Rev. B **84**, 035301 (2011).
- [4] L. Fang, Y. Jia, D. J. Miller, M. L. Latimer, Z. L. Xiao, U. Welp, G. W. Crabtree, and W. K. Kwok, *Catalyst-Free Growth of Millimeter-Long Topological Insulator Bi_2Se_3 Nanoribbons and the Observation of the π -Berry Phase*, Nano Lett. **12**, 6164 (2012).
- [5] Y. Y. Lv *et al.*, *Shubnikov–de Haas oscillations in bulk ZrTe_5 single crystals: Evidence for a weak topological insulator*, Phys. Rev. B **97**, 115137 (2018).
- [6] L. Fu, C. L. Kane, and E. J. Mele, *Topological Insulators in Three Dimensions*, Phys. Rev. Lett. **98**, 106803 (2007).
- [7] M. Z. Hasan and C. L. Kane, *Colloquium: Topological insulators*, Rev. Mod. Phys. **82**, 3045 (2010).
- [8] Y. Ando, *Topological Insulator Materials*, J. Phys. Soc. Japan **82**, 102001 (2013).
- [9] C. X. Liu, X. L. Qi, H. J. Zhang, X. Dai, Z. Fang, and S. C. Zhang, *Model Hamiltonian for topological insulators*, Phys. Rev. B **82**, 045122 (2010).
- [10] Y. L. Chen *et al.*, *Experimental Realization of a Three-Dimensional Topological Insulator, Bi_2Te_3* , Science **325**, 178 (2009).
- [11] H. Zhang, C. X. Liu, X. L. Qi, X. Dai, Z. Fang, and S. C. Zhang, *Topological insulators in Bi_2Se_3 , Bi_2Te_3 and Sb_2Te_3 with a single Dirac cone on the surface*, Nat. Phys. **5**, 438 (2009).
- [12] Z. Wang, Y. Sun, X. Q. Chen, C. Franchini, G. Xu, H. Weng, X. Dai, and Z. Fang, *Dirac semimetal and topological phase transitions in A_3Bi ($\text{A}=\text{Na}, \text{K}, \text{Rb}$)*, Phys. Rev. B **85**, 195320 (2012).
- [13] B. Q. Lv *et al.*, *Experimental Discovery of Weyl Semimetal TaAs*, Phys. Rev. X **5**, 031013 (2015).
- [14] B. J. Yang and N. Nagaosa, *Classification of stable three-dimensional Dirac semimetals with non-trivial topology*, Nat. Commun. **5**, 4898 (2014).

- [15] N. P. Armitage, E. J. Mele, and A. Vishwanath, *Weyl and Dirac semimetals in three-dimensional solids*, Rev. Mod. Phys. **90**, 15001 (2018).
- [16] A. Burkov, *Topological semimetals*, Nat. Mater. **15**, 1145 (2016).
- [17] S.-Y. Xu *et al.*, *Observation of Fermi arc surface states in a topological metal*, Science **347**, 294 (2015).
- [18] L. P. He, X. C. Hong, J. K. Dong, J. Pan, Z. Zhang, J. Zhang, and S. Y. Li, *Quantum Transport Evidence for the Three-Dimensional Dirac Semimetal Phase in Cd_3As_2* , Phys. Rev. Lett. **113**, 246402 (2014).
- [19] F. Orbančić, M. Novak, M. Baćani, and I. Kokanović, *Quantum oscillations in a lead chalcogenide three-dimensional Dirac system*, Phys. Rev. B **95**, 035208 (2017).
- [20] F. Tang *et al.*, *Three-dimensional quantum Hall effect and metal–insulator transition in $ZrTe_5$* , Nature **569**, 537 (2019).
- [21] Z. J. Xiang, D. Zhao, Z. Jin, C. Shang, L. K. Ma, G. J. Ye, B. Lei, T. Wu, Z. C. Xia, and X. H. Chen, *Angular-Dependent Phase Factor of Shubnikov–de Haas Oscillations in the Dirac Semimetal Cd_3As_2* , Phys. Rev. Lett. **115**, 226401 (2015).
- [22] J. Hu, J. Y. Liu, D. Graf, S. M. A. Radmanesh, D. J. Adams, A. Chuang, Y. Wang, I. Chiorescu, J. Wei, L. Spinu, and Z. Q. Mao, *π Berry phase and Zeeman splitting of Weyl semimetal TaP* , Sci. Rep. **6**, 18674 (2016).
- [23] P. Sergelius *et al.*, *Berry phase and band structure analysis of the Weyl semimetal NbP* , Sci. Rep. **6**, 33859 (2016).
- [24] G. P. Mikitik and Y. V. Sharlaĭ, *Semiclassical energy levels of electrons in metals with band degeneracy lines*, J. Exp. Theor. Phys. **87**, 747 (1998).
- [25] D. Shoenberg, *Magnetic Oscillations in Metals* (Cambridge University Press, Cambridge, England, 1984).
- [26] A. Alexandradinata, C. Wang, W. Duan, and L. Glazman, *Revealing the Topology of Fermi-Surface*

- Wave Functions from Magnetic Quantum Oscillations*, Phys. Rev. X **8**, 11027 (2018).
- [27] Q. Li, D. E. Kharzeev, C. Zhang, Y. Huang, I. Pletikosić, A. V. Fedorov, R. D. Zhong, J. A. Schneeloch, G. D. Gu, and T. Valla, *Chiral magnetic effect in ZrTe₅*, Nat. Phys. **12**, 550 (2016).
 - [28] T. Liang *et al.*, *Anomalous Hall effect in ZrTe₅*, Nat. Phys. **14**, 451 (2018).
 - [29] Y. Liu *et al.*, *Zeeman splitting and dynamical mass generation in Dirac semimetal ZrTe₅*, Nat. Commun. **7**, 12516 (2016).
 - [30] J. Wang, J. Niu, B. Yan, X. Li, R. Bi, Y. Yao, D. Yu, and X. Wu, *Vanishing quantum oscillations in Dirac semimetal ZrTe₅*, Proc. Natl. Acad. Sci. U. S. A. **115**, 9145 (2018).
 - [31] H. Weng, X. Dai, and Z. Fang, *Transition-Metal Pentatelluride ZrTe₅ and HfTe₅: A Paradigm for Large-Gap Quantum Spin Hall Insulators*, Phys. Rev. X **4**, 011002 (2014).
 - [32] K. Wang, D. Graf, L. Li, L. Wang, and C. Petrovic, *Anisotropic giant magnetoresistance in NbSb₂*, Sci. Rep. **4**, 7328 (2014).
 - [33] L. Guo *et al.*, *Extreme magnetoresistance and SdH oscillation in compensated semimetals of NbSb₂ single crystals*, J. Appl. Phys. **123**, 155103 (2018).
 - [34] C. Xu, J. Chen, G. X. Zhi, Y. Li, J. Dai, and C. Cao, *Electronic structures of transition metal dipnictides XPn₂ (X = Ta, Nb; Pn = P, As, Sb)*, Phys. Rev. B **93**, 195106 (2016).
 - [35] E. N. Adams and T. D. Holstein, *Quantum Theory of Transverse Galvano-Magnetic Phenomena*, J. Phys. Chem. Solids **10**, 254 (1959).
 - [36] I. A. Leahy, Y. P. Lin, P. E. Siegfried, A. C. Treglia, J. C. W. Song, R. M. Nandkishore, and M. Lee, *Nonsaturating large magnetoresistance in semimetals*, Proc. Natl. Acad. Sci. U. S. A. **115**, 10570 (2018).
 - [37] M. N. Ali *et al.*, *Large, nonsaturating magnetoresistance in WTe₂*, Nature **514**, 205 (2014).
 - [38] C. Shekhar *et al.*, *Extremely large magnetoresistance and ultrahigh mobility in the topological weyl semimetal candidate NbP*, Nat. Phys. **11**, 645 (2015).

- [39] Z. Yuan, H. Lu, Y. Liu, J. Wang, and S. Jia, *Large magnetoresistance in compensated semimetals TaAs₂ and NbAs₂*, Phys. Rev. B **93**, 184405 (2016).
- [40] C. M. Wang, H. Z. Lu, and S. Q. Shen, *Anomalous Phase Shift of Quantum Oscillations in 3D Topological Semimetals*, Phys. Rev. Lett. **117**, 077201 (2016).
- [41] M. H. Cohen and E. I. Blount, *The g-factor and de Haas-van Alphen Effect of Electrons in Bismuth*, Philos. Mag. **5**, 115 (1960).
- [42] A. Pariari, R. Singha, S. Roy, B. Satpati, and P. Mandal, *Anisotropic transverse magnetoresistance and Fermi surface in TaSb₂*, Sci. Rep. **8**, 10527 (2018).